

Mathematical Neuroscience - Assignment 2

Ca^{2+} currents and Bursting

Matiš Halák - 2724858 (VU Student ID)

March, April 2025

1 L-type Ca^{2+} currents

For this section we investigate a minimal neuronal model with L-type ("long-lasting") calcium currents, defined as:

$$\begin{aligned}\frac{dv}{dt} &= I_{\text{app}} - g_L(V - E_L) - I_{C_a,L}(V, C_a) \\ \frac{dC_a}{dt} &= -\beta I_{C_a,L}(V, C_a) - \frac{C_a - C_a^\infty}{\tau_{C_a}}\end{aligned}$$

where C_a represents intracellular calcium concentration and V represents the membrane voltage.

1.1 Calcium dynamics equation

The calcium dynamics equation, $\frac{dC_a}{dt} = -\beta I_{C_a,L}(V, C_a) - \frac{C_a - C_a^\infty}{\tau_{C_a}}$, consists of two terms. The first term ($-\beta I_{C_a,L}(V, C_a)$) means that the change in intracellular calcium depends on the L-type calcium current. Specifically, if the calcium current $I_{C_a,L}$ is passing into the cell (according to the electrophysiology convention, the inward current $I_{C_a,L} < 0$), this term will push the calcium concentration in the cell to increase. On the other hand, if calcium ions are leaving the cell (outward current, $I_{C_a,L} > 0$), the calcium concentration in the cell will decrease. β is a factor that translates ionic current from the charge per unit time into the concentration per unit time timescale. Because $I_{C_a,L}(V, C_a)$ depends on voltage, term 1 can be seen as the voltage-dependent term of the calcium dynamics equation.

The second term ($-\frac{C_a - C_a^\infty}{\tau_{C_a}}$) means that change in intracellular calcium also depends on the current levels of intracellular calcium. In particular, when $C_a > C_a^\infty$, the calcium concentration inside the cell will start to decrease to bring calcium back to C_a^∞ . In contrast, when $C_a < C_a^\infty$, the cell will try to increase internal calcium to bring it to the level C_a^∞ . Therefore, term 2 represents a homeostatic mechanism that restores calcium to baseline (C_a^∞) levels, probably through calcium pumps or exchangers. Since term 2 only depends on intracellular calcium levels, it can be seen as the calcium-dependent term of the calcium dynamics equation.

As $\beta = 0.01$, and $\frac{1}{\tau_{C_a}} = 0.005$, term 2 responds slower to changes in calcium concentration than term 1 responds to changes in membrane voltage and current influx. This makes sense since homeostatic mechanisms like the one captured by term 2 are typically slow (active transport through pumps and exchangers is slower than rapid influx through channels) and serve mainly to protect the cell from abnormal calcium levels for prolonged periods of time.

Terms 1 and 2 are competing because upon large calcium influx through L-type calcium channels, term 1 will be > 0 , while term 2 will be < 0 . However, because term 2 evolves on a slower time scale, calcium removal will lag behind the calcium influx described by term 1 and the equation for $\frac{dv}{dt}$. Therefore, while calcium influx through L-type calcium channels is fast, calcium concentration-dependent calcium removal from the cell is slow.

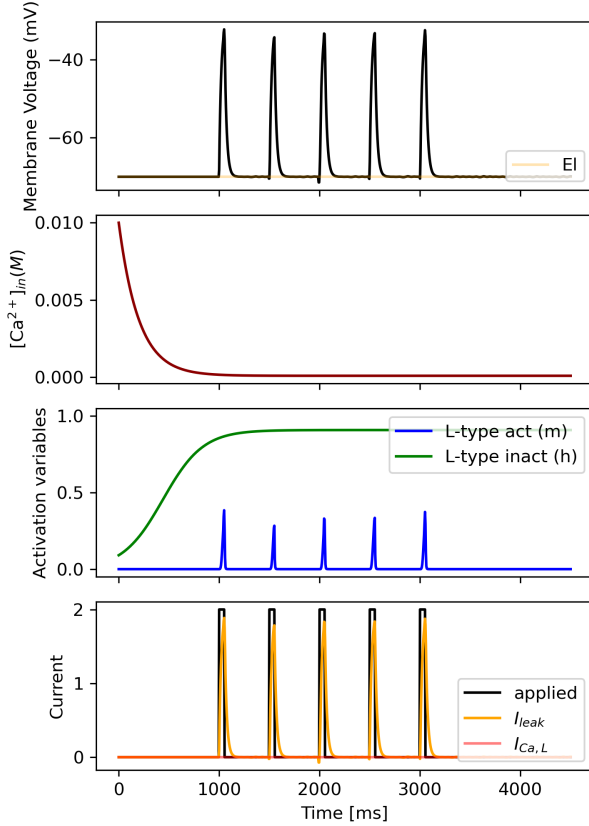


Figure 1: Decoupled passive membrane system at $P_{max} = 0$

1.2 System dynamics in absence of L-type Ca^{2+} current

When we set $P_{max} = 0$ (i.e. by blocking L-type calcium channels) in this simple model, the voltage and calcium concentration will become decoupled and independent - dv/dt can no longer sense and respond to Ca and $d\text{Ca}/dt$ can no longer sense and respond to V. The voltage equation becomes $\frac{dv}{dt} = I_{app} - g_L(V - E_L)$, which represents a passive membrane that always returns to E_L equilibrium potential after I_{app} is removed. With only the leak current left, this system is unable to produce oscillations or even spikes. Instead, the voltage will always peak when current is applied (proportionally to the strength of the applied current) and decay to E_L afterwards. The calcium equation becomes $\frac{dC_a}{dt} = -\frac{C_a - C_{a\infty}}{\tau_{C_a}}$, which means that regardless of the initial Ca level, the cell will slowly return to the baseline $C_{a\infty}$ and stay in this equilibrium. The described behaviors are captured in a Python simulation shown in Figure 1.

1.3 Instantaneous activation of L-type Ca^{2+} channels

We can say that L-type channel activation is instantaneous because the activation gate m does not have its own differential equation and is instead calculated immediately from the membrane voltage at each $V(t)$ with $m(V) = m_\infty(V)$. For this to be possible, the assumption is that m tracks $V(t)$ instantaneously, and that at any $V(t)$ we can know what the immediate $m(V)$ will be based on the $m_\infty(V)$ function.

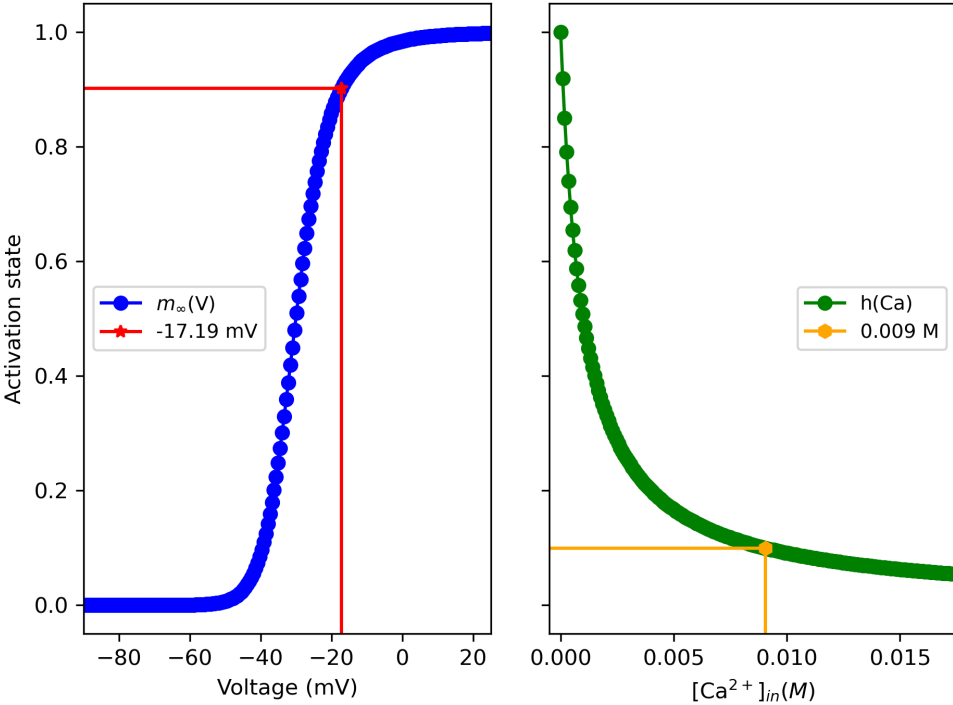


Figure 2: Activation ($m_\infty(V)$) and inactivation ($h(\text{Ca})$) gating curves of L-type calcium channels.

1.4 Gating of L-type Ca^{2+} channels

We show the activation and inactivation gating curves for L-type calcium channels in Figure 2. These were obtained using a custom-written Python script. This allows us to complete S1 and S2:

S1: at -17.19 mV 90% of L-type calcium channels are activated; $m(-17.19 \text{ V}) = 0.9$.

S2: at 0.009 M 90% of L-type calcium channels are inactivated; $h(0.009 \text{ M}) = 0.1$.

As -17.19 mV is quite a high voltage threshold (e.g. much higher than the typical -55 mV for N_{a_v}) and 0.009 is a high calcium concentration, these numbers match the expected high activation and high inactivation thresholds for L-type calcium channels.

1.5 Phase portrait of L-type current model with $I_{app}(t) \equiv 1$ (and across I_{app})

Here we investigated the phase plane of the L-type model obtained using a custom-written Python script. We first chose a range for both V and Ca to see both nullclines (for other analyses, we sometimes restricted the range to biologically plausible bounds). For each parameter combination, we calculated the derivative for that variable at that point for fixed $I_{app}(t)$. The nullcline for each variable was found as the regions in the phase plane with derivative = 0. The exact equilibrium point was found using `fsoolve`, with the initial guess being chosen as the coordinate for both variables that minimized the Sum of Squares of their derivatives. We also characterized the stability and nature of equilibria at each I_{app} using small perturbations to estimate the Jacobian at each equilibrium point. We confirmed that this method nicely tracked the shifting location and nature of equilibria and nullclines, at least in the range $I_{app}(t) \in (0, 6)$ (see Animation 1). The resulting phase plane with equilibrium, nullclines and direction of derivatives at 40,000 parameter combinations for $I_{app}(t) \equiv 1$ is shown in Figure 3.

The equilibrium found in this regime, $E(I_{app} \equiv 1) = (V_*, Ca_*) = (-47.033, 0.297)$ is a stable focus (meaning the Jacobian at this point has a negative trace and complex eigenvalues). With our investigation

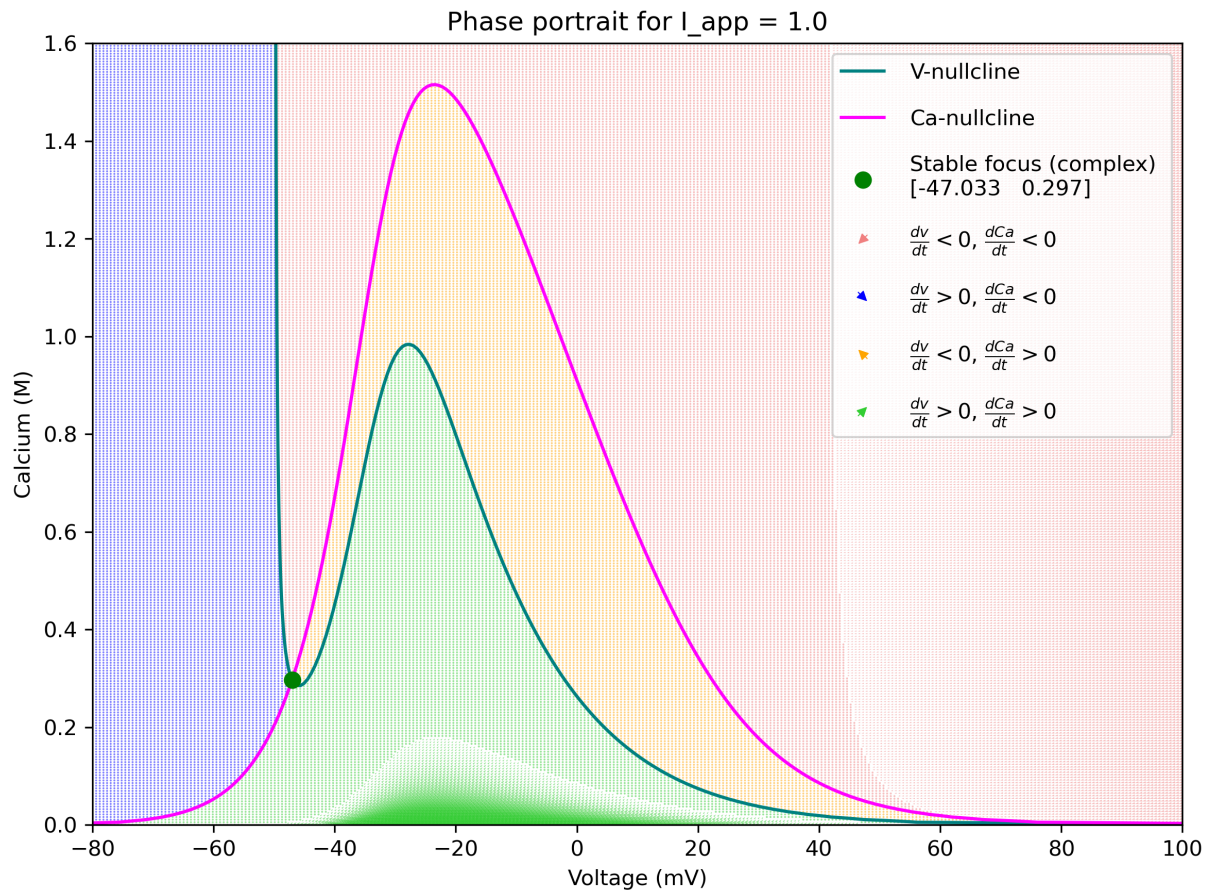


Figure 3: Phase plane of L-type current model. The phase portrait contains 40,000 small arrows with different directions and colors, each indicating the $\frac{dV}{dt}$, $\frac{dCa}{dt}$ at that (V, Ca) state of the system. Equilibrium is highlighted as a point (green if stable, red if unstable, with coordinates in legend).

of the phase plane across I_{app} (Animation 1) we saw that with increasing applied current (range 0,6), the nature and stability of the equilibrium changes from Stable node - Stable focus - Unstable focus - Stable focus - Stable node, already indicating that the system undergoes bifurcations in this range in this range of applied current.

1.6 L-type current model behavior and bifurcations

1.6.1 State transitions upon application of instantaneous switch current

To obtain evidence to support S3, we performed custom python simulations across a range of I_{app} from 0-3, starting from 4 different initial conditions (one in each quadrant of the phase plane divided by the V and Ca nullclines) (see (Animation 2). Representative examples for each case (i, ii, iii) from S3 are shown in Figure 4. We chose time of applying switch current to be 1600, because that allowed all 4 initial conditions to settle to the equilibrium at the initial $I_{app} = 0$.

Case i) New steady state without emitting a spike ($I_{app} = 0.2308$ if $t \geq 1600$ else 0)(Figure 4a, 4b). In this case, the current switch just slightly bumps up the voltage, by approaching the new stable node equilibrium from the left side (without crossing the middle or right branches of the V-nullcline).

Case ii) New steady state after emitting a spike ($I_{app} = 1$ if $t \geq 1600$ else 0)(Figure 4c, 4d). Here we see the current switch results in a large excursion through phase space, all the way through the right branch of the V-nullcline, before settling at a higher equilibrium voltage at the stable focus equilibrium. Because this excursion goes right of the middle and right branches of the V-nullcline before wrapping back left towards the equilibrium, we consider this to be a spike (and also the voltage trace looks like a spike).

Case iii) New steady state is a stable periodic orbit ($I_{app} = 1.2308$ if $t \geq 1600$ else 0)(Figure 4e, 4f). Finally, we see the case where after emitting an initial spike (trajectory passes both middle and right branch of V-nullcline), the system settles into a periodic orbit of sustained spiking. This happens (as discussed in the next section) because the stable focus equilibrium from before (eg. $I_{app} = 1$) loses stability and a stable periodic orbit appears via a Hopf bifurcation.

1.6.2 Bistability with constantly applied I_{app}

For this section, we first attempted to analyze the bifurcations using custom-written Python code, but eventually we reverted to MatCont. In previous analyses, we already discovered that the equilibrium becomes unstable and is surrounded by a periodic orbit when $I_{app} \in (1.1, 1.3)$. We saw this back nicely in both Python and MatCont initial bifurcation diagrams and proceeded to investigate this further with MatCont. We were able to find the full periodic orbit, as well as a number of bifurcations in the range of interest (Figure 5).

The first bifurcation detected at $I_{app} = 1.1279$ is a Subcritical Hopf bifurcation (first Lyapunov coefficient > 0). Another Hopf bifurcation was found at $I_{app} = 1.2822$, this time a Supercritical Hopf bifurcation (first Lyapunov coefficient < 0). These bifurcations nicely border the limit cycle observed in the bifurcation diagram (Figure 5a), and also experimentally in simulations and in the phase plane. The sequence of events around the limit cycle might go as follows.

At $I_{app} = 1.28$, as I_{app} decreases (moving right to left) the stable branch of equilibria become unstable and a stable (blue) limit cycle emerges, matching the characteristics of the Supercritical Hopf bifurcation that occurs there. Subsequently, (still moving from right to left) in Figure 5b, we see that a small unstable (red) limit cycle appears at the Subcritical Hopf ($I_{app} = 1.1279$), and we see that this is also where the branch of unstable equilibria regain stability, which matches the sequence of events in a Subcritical Hopf bifurcation if followed from the unstable branch in the direction of the unstable limit cycle. Unfortunately, it is unclear to me how the LPC and BPC points fall into this picture.

Based on the phase plane analysis and the simple bifurcation diagram in Figure 5a and the process described above, I would argue that the L-type model does not support bistability at any point, instead it switches from stable branch of equilibria to a stable limit cycle and back to a stable branch of equilibria.

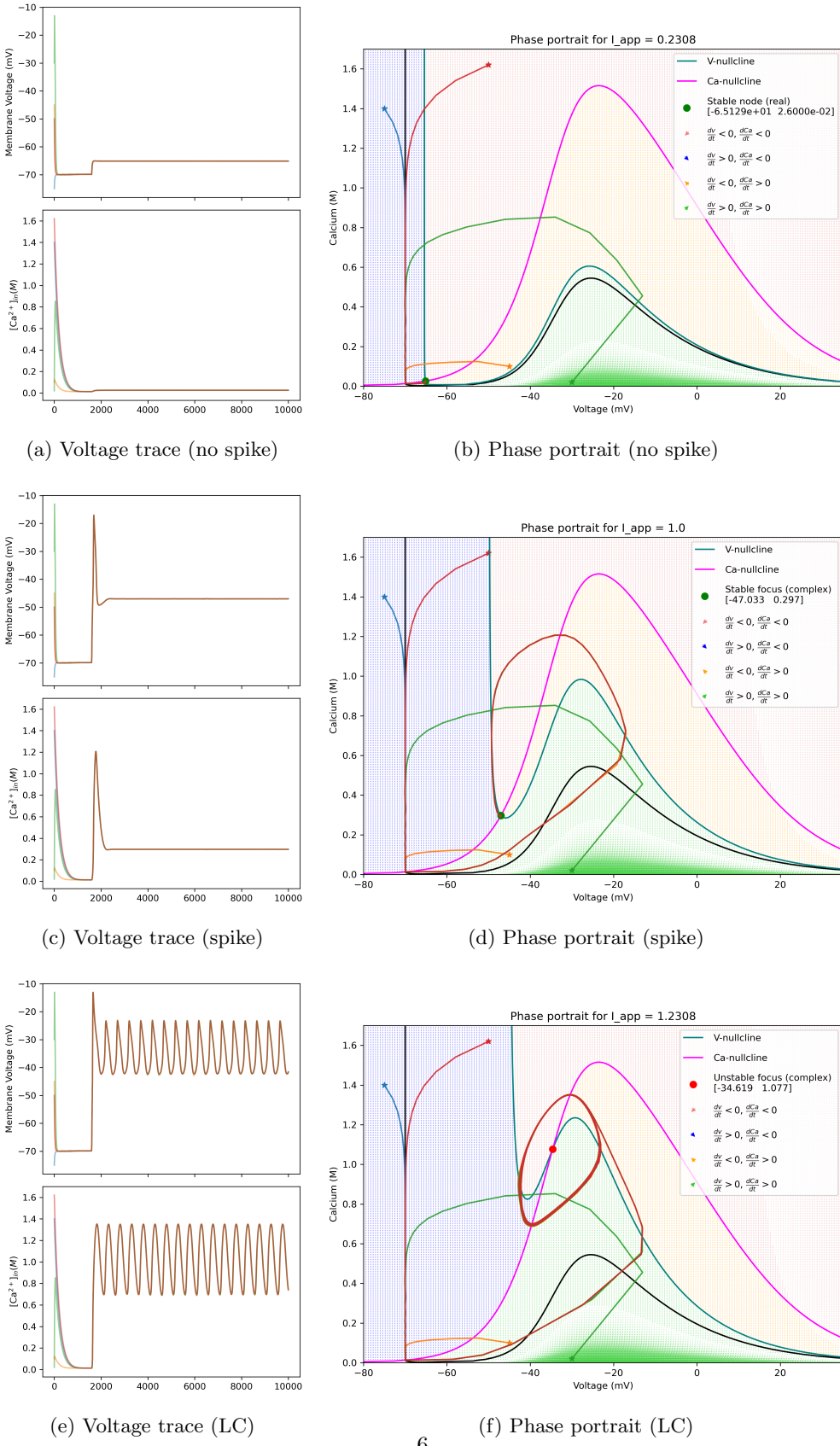


Figure 4: L-type model across applied currents. **Left:** Voltage and Calcium traces over time; **Right:** Phase portraits observed trajectories. **Top:** New steady state WITHOUT spike; **Middle:** New steady state AFTER spike; **Bottom:** New steady state IS stable periodic orbit. V -nullcline at $I_{app} = 0$ in black.

2 Bursting in Morris-Lecar model

In this section we discuss the Morris-Lecar Burster model defined as:

$$\begin{aligned} C_m \frac{dV}{dt} &= I_{\text{app}} - g_L(V - E_L) - g_K n(V - E_K) - g_{Ca} m_\infty(V)(V - E_{Ca}) - I_{KCa}(V, Ca) \\ \frac{dn}{dt} &= \phi(n_\infty(V) - n)/\tau_n(V) \\ \frac{dCa}{dt} &= \epsilon(-\mu I_{Ca}(V) - k_{Ca} Ca) \end{aligned}$$

All plots and code for this section were custom written in Python.

2.1 Equilibria of the Morris-Lecar model

We first define the fast subsystem as:

$$\begin{aligned} C_m \frac{dV^*}{dt} &= I_{\text{app}} - g_L(V^* - E_L) - g_K n^*(V^* - E_K) - g_{Ca} m_\infty(V^*)(V^* - E_{Ca}) - I_{KCa}(V^*, Ca) \\ \frac{dn^*}{dt} &= \phi(n_\infty(V^*) - n^*)/\tau_n(V^*) \end{aligned}$$

where the slow Ca is a parameter. The equilibria for this fast sub-system can be seen in Figure 6 to form a Z-shaped curve, which has been cut-off at $[Ca] = 2$ to stay within physiological [Ca] range.

To derive the $d[Ca]/dt = 0$ manifold, we manipulated the $d[Ca]/dt$ equation to obtain:

$$Ca = \frac{-\mu}{k_{Ca}} I_{Ca}(V)$$

where $I_{Ca}(V) = g_{Ca} m_\infty(V)(V - E_{Ca})$. This gives a 2D manifold (G) in Ca and V, which is identical for any value of n (see Figure 6).

Since all points on the manifold G have $d[Ca]/dt = 0$, and all the points on the fast-subsystem equilibrium curve have $dV/dt = dn/dt = 0$, the intersection points between this manifold and the curve will have $d[Ca]/dt = dV/dt = dn/dt = 0$, which is by definition an equilibrium of the full system. We note that the intersection of G and the fast-subsystem equilibria happens at the "knee" joining the lower and middle branches of the fast subsystem equilibria curve.

2.2 Simulation of Morris-Lecar Model

A simple Python simulation of the model with default parameters yielded nice bursting behavior, exemplified by the time-series traces in Figure 7a. Comparing to the square-wave burster example from the book, we see that our model also shows square-like bursts in their shape, with depolarized voltage throughout the active bursting phase and frequency of firing slowing down towards the end of the active bursting phase.

In Figure 7b we can see the trajectory in (Ca, n, V) space of the three consecutive bursts that we observed. Interpreting the trajectory in terms of square-wave bursting, we see that the trajectory oscillates around the unstable upper branch of equilibria of the fast subsystem, before returning to the stable lower branch of the fast subsystem along which it continues until it reaches the saddle at the joining of the lower and middle equilibrium branch (equilibrium of the full system) and is shot back up into the bursting phase via a saddle-node bifurcation.

2.3 Effective change of $[Ca^{2+}]$ along periodic orbit

For this question I used the fast sub-system, as defined in Section 2.1. And followed the outlined steps to produce the function H(Ca) shown in Figure 8 and find Ca^* where $H = 0$.

2.4 Characteristics of H

From Figure 8 we see that H is a decreasing function of $[Ca]$. In the simulation, there were perhaps some numerical instabilities that resulted in noise at some of the low calcium levels which make the curve not smooth. We find $Ca^* = 0.5859$, after which, even in our simulation, H is a monotonously decreasing function of $[Ca]$. This means that for $[Ca] < Ca^*$ calcium increases along the periodic orbits but for $[Ca] < Ca^*$ calcium just keeps decreasing .

2.5 ϵ and tonic firing versus square-wave bursting

First, manifold G ($d[Ca]/dt = 0$ manifold) is not affected by epsilon levels, as can be seen in the equation that defines it in Section 2.1. However, as can be seen in Figure 9, there are key differences between the tonic spiking trajectories at low ϵ (eg. $\epsilon = 0.0007$) and the bursting trajectories at higher epsilon ϵ (eg. $\epsilon = 0.002$).

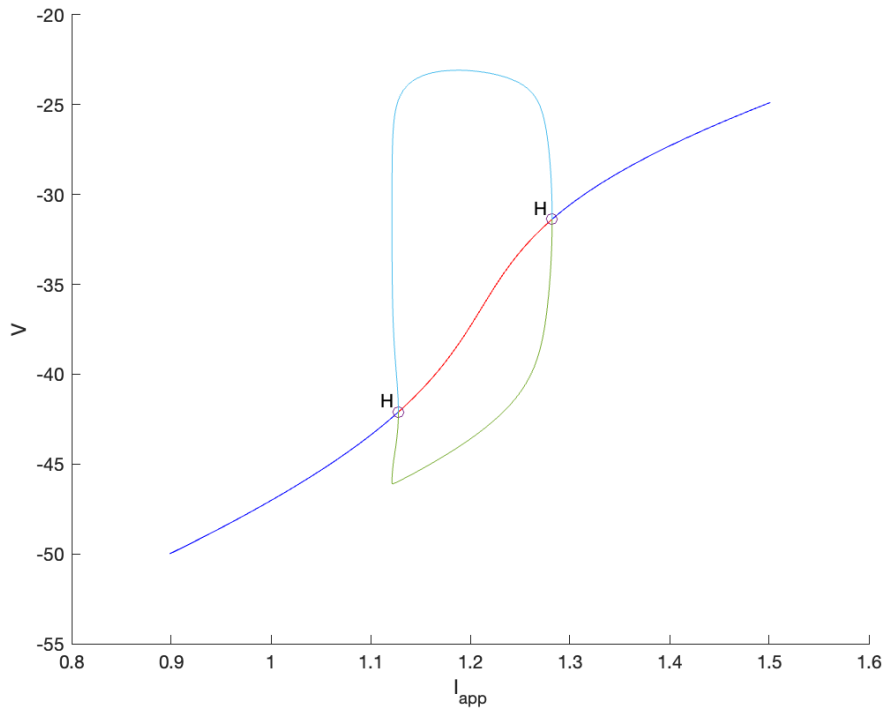
That is, at low ϵ we see that the solutions stay above G and never return to the lower equilibrium branch of the fast subsystem and are therefore stuck in a tonic firing pattern. What is notable is that while the $H(Ca)$ curve has the same shape, it is significantly scaled down at lower ϵ (Figure 9a, meaning that the effective change in $[Ca]$ along one spike is so negligible that it cannot throw the system out of tonic spiking beyond $[Ca]^h$. The lack of effect of the overly slow calcium influence on the fast variables can also be seen when looking at the Voltage and Calcium time series traces in Figure 9b. In contrast, at high ϵ we see that solutions eventually cross $[Ca]^h$, stop bursting and return to the lower equilibrium branch of the fast subsystem below G , along which they drift where $H(Ca) < 0$ and $[Ca]$ keeps decreasing until the system reaches a saddle-node bifurcation and the system reenters the spiking / bursting manifold (Figure 9e). Because $H(Ca)$ is scaled up, the calcium effects are sufficiently fast and strong to push the system over $[Ca]^h$.

Therefore, ϵ controls how much the slow variable $[Ca]$ can be moved by a set of spikes within the fixed geometry of G and fast-subsystem equilibria. If a set of spikes can move $[Ca]$ beyond $[Ca]^h$ then the system will exhibit bursting, otherwise it will settle into tonic spiking just before $[Ca]^h$, never being able to reach it.

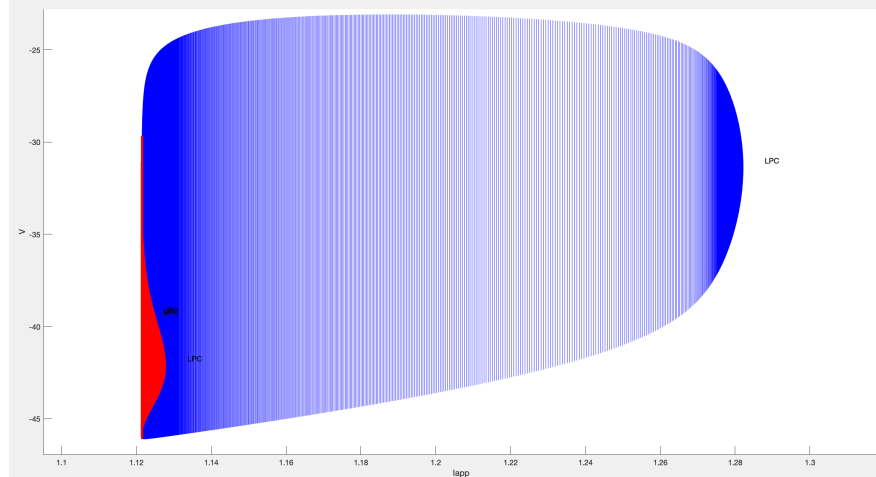
2.6 Homeostasis rate μ

Finally, we investigate the effect of increasing the homeostasis rate μ . From the definition of, manifold G ($d[Ca]/dt = 0$ manifold, Section 2.1), we can immediately see that it will be directly affected by changes in μ . Accordingly, we observe that when elevating μ to 0.06, the entire G manifold shifts down along the voltage axis (Figure 10b). The effect of this is that the intersection between G and the fast-subsystem equilibria now happens along the stable, lower branch of equilibria of the fast subsystem and not at the knee joining the lower and middle branches. Because this point is not also a stable equilibrium branch for the fast subsystem, the solutions will just stay here forever (also see Figure 10a for one burst and stabilization at steady state). Contrast this with the previously seen cases at lower μ where the equilibrium of the full system intersected a saddle in the fast-subsystem which resulted in shooting up the solutions back into the bursting manifold via a saddle-node bifurcation (eg. Figure 7b).

Therefore, μ controls the position of the G manifold and therefore also the location and nature of the equilibria of the full system. If G intersects the fast-subsystem equilibria exactly at the knee joining the lower and middle branches ($\mu = 0.02$), bursting can occur, as the trajectories arriving at this semi-stable full equilibrium (after one full burst) will have no choice but to jump back into the bursting manifold and continue repeating this bursting cycle forever (eg. Figure 9f). In contrast, if G intersects the lower branch of the fast-subsystem equilibria ($\mu > 0.02$), after giving out one burst, the solutions stabilize at steady state at the intersection of the lower branch and G (Figure 10).



(a) Bifurcation diagram of L-type model



(b) Limit cycle in L-type model

Figure 5: Bifurcation in L-type model. Plot shows relevant range around detected bifurcations.

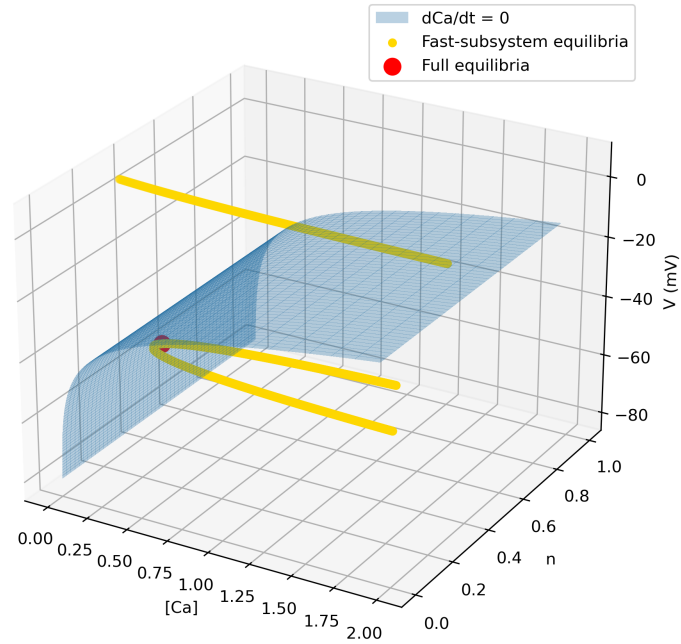


Figure 6: Fast subsystem equilibria (yellow) and $d[Ca]/dt = 0$ manifold (blue)

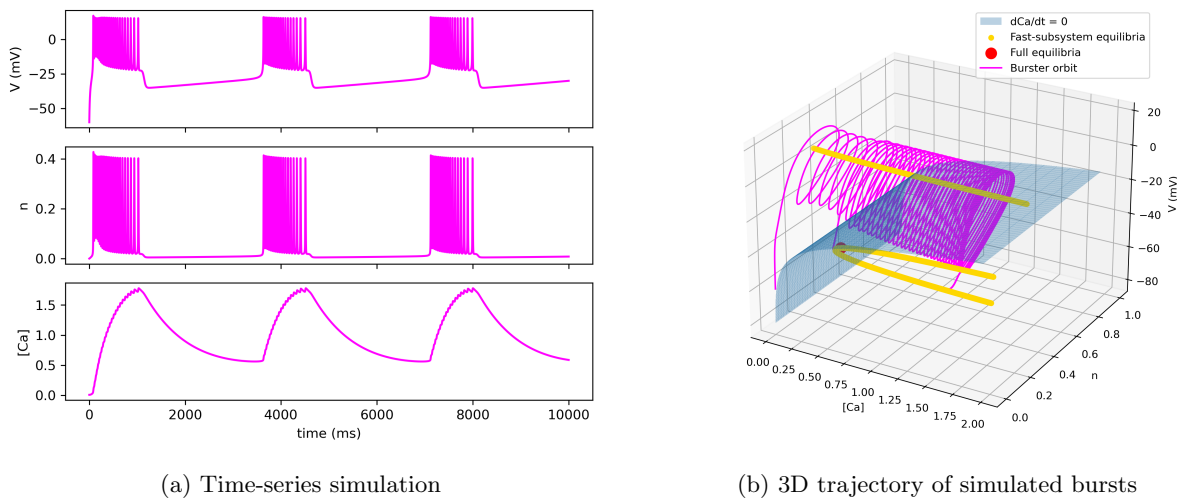


Figure 7: Simulation of MLburst model with default parameters.

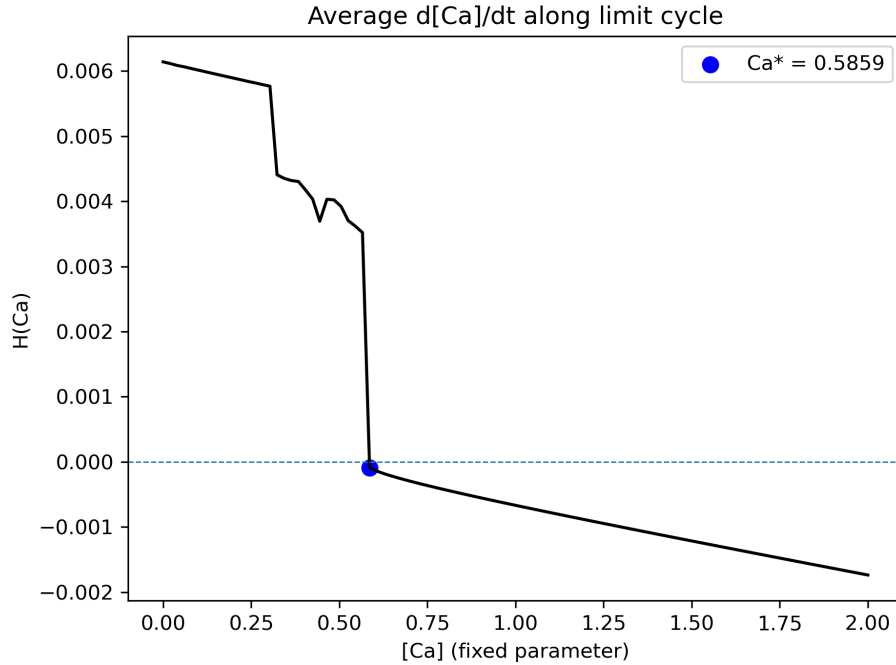


Figure 8: Effective change of $[\text{Ca}]$ along one periodic orbit ($\epsilon = 0.001$)

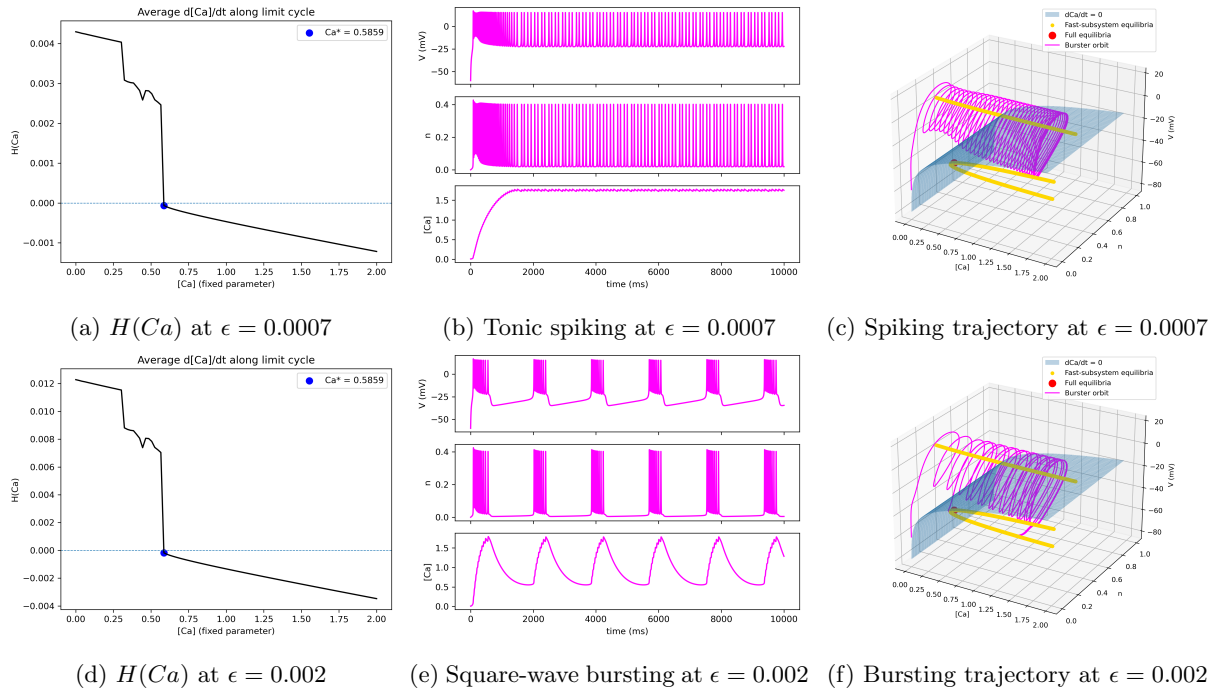
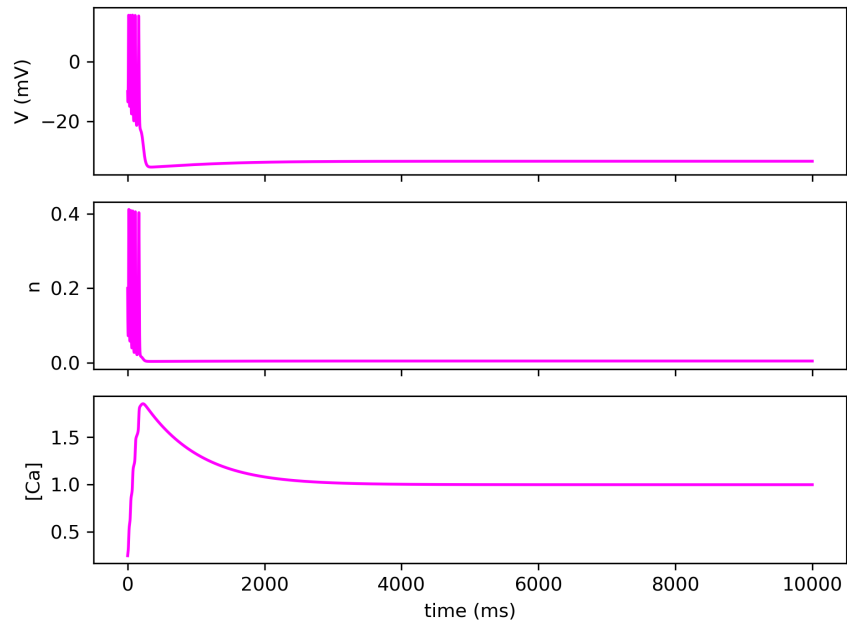
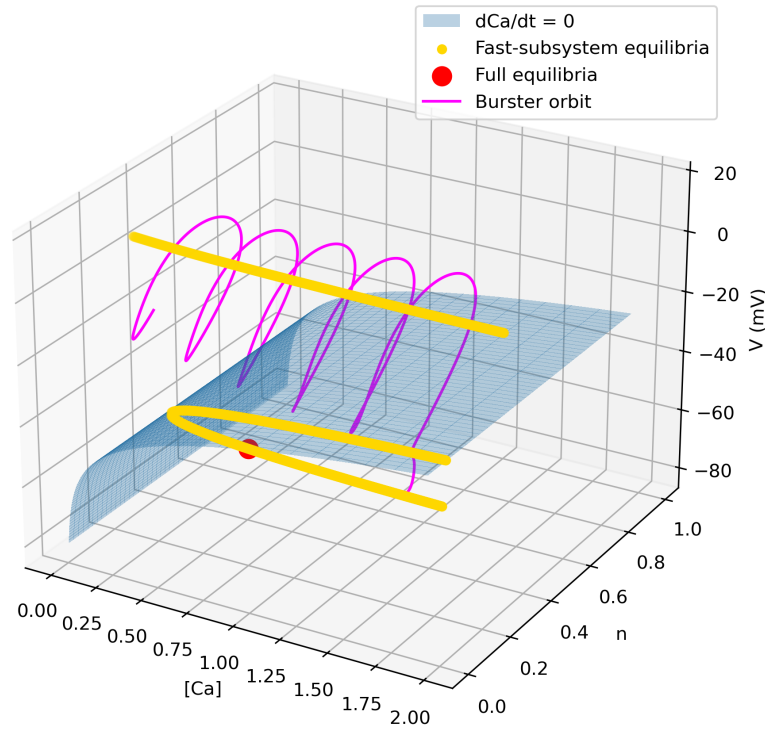


Figure 9: Tonic spiking (low ϵ) vs square-wave bursting (high ϵ)



(a) Time-series simulation at $\mu = 0.06$



(b) 3D trajectory at $\mu = 0.06$

Figure 10: Simulation of MLburst model with increased $\mu = 0.06$.